

Reinforcement Learning for SAR View Angle Inversion with Differentiable SAR Renderer

Yanni Wang, *Graduate Student Member, IEEE*, Hecheng Jia, *Graduate Student Member, IEEE*, Shilei Fu, *Graduate Student Member, IEEE*, Huiping Lin, *Member, IEEE*, Feng Xu, *Senior Member, IEEE*

Abstract—The electromagnetic inverse problem has long been a research hotspot. This study aims to reverse radar view angles in synthetic aperture radar (SAR) images given a target model. Nonetheless, the scarcity of SAR data, combined with the intricate background interference and imaging mechanisms, limit the applications of existing learning-based approaches. To address these challenges, we propose an interactive deep reinforcement learning (DRL) framework, where an electromagnetic simulator named differentiable SAR render (DSR) is embedded to facilitate the interaction between the agent and the environment, simulating a human-like process of angle prediction. Specifically, DSR generates SAR images at arbitrary view angles in real time. And the differences in sequential and semantic aspects between the view angle-corresponding images are leveraged to construct the state space in DRL, which effectively suppress the complex background interference, enhance the sensitivity to temporal variations, and improve the capability to capture fine-grained information. Additionally, in order to maintain the stability and convergence of our method, a series of reward mechanisms, such as memory difference, smoothing and boundary penalty, are utilized to form the final reward function. Extensive experiments performed on both simulated and real datasets demonstrate the effectiveness and robustness of our proposed method. When utilized in the cross-domain area, the proposed method greatly mitigates inconsistency between simulated and real domains, outperforming reference methods significantly.

Index Terms—Deep reinforcement learning (DRL), differentiable SAR render (DSR), synthetic aperture radar (SAR), radar view angles

I. INTRODUCTION

ELECTROMAGNETIC inverse problem focuses on inferring the properties of the target and the sensor’s observational characteristics, given the known attributes of the target. Synthetic aperture radar (SAR) functions as an active remote sensing sensor that operates within the microwave frequency spectrum, boasting capabilities for round-the-clock and all-weather operation [1]. The inversion of radar observation angles in SAR imagery remains a central electromagnetic inverse challenge. This task aims to ascertain the radar view angles of targets within the radar coordinate system from a supplied SAR image, which has critical implications for fields ranging from radar imaging and monitoring [2] to intelligent transportation [3] and environmental monitoring [4].

This work was supported in part by the National Natural Science Foundation of China under Grant U2130202, and in part by the Fundamental Research Funds for the Central Universities. (*Corresponding Authors: Huiping Lin, Feng Xu*).

The authors are with the Key Laboratory for Information Science of Electromagnetic Waves (MoE), Fudan University, Shanghai 200433, China. (email: fengxu@fudan.edu.cn)

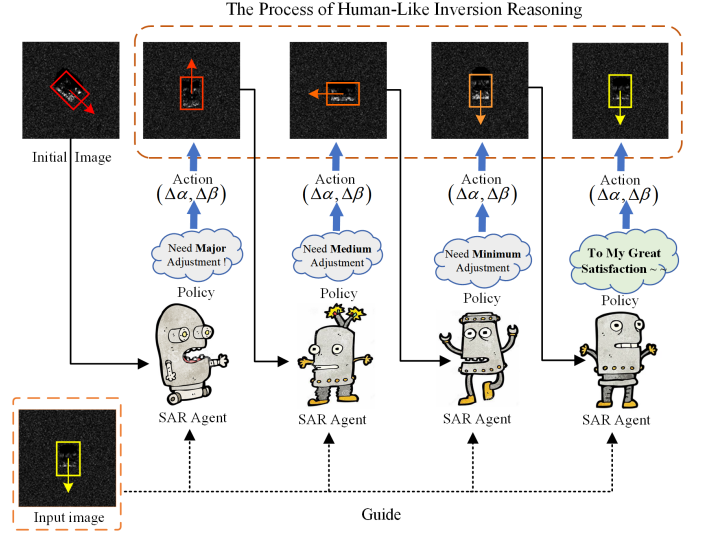


Fig. 1. The SAR agent learns inverse policies and takes actions to reverse view angles of SAR image from any arbitrary, mirroring the decision-making process similar to human prediction. Due to the diverse range of view angles, the SAR agents are required to employ actions with varying adjustments based on the disparity between the reference and current inversion SAR image.

However, various imaging factors like multiple scattering phenomena, intricate background disturbances, shadowing effects and speckle noise hinder the view angle inversion process [5].

Most existing methods [6], [7], [8] utilize traditional optimization techniques to address inverse problems, incorporating both gradient-based and heuristic optimization algorithms. Gradient-based methods are particularly suited to problems with available gradient information and a finite solution space. However, in discrete domains with high dimensions, the necessity for robustness intensifies. Heuristic algorithms, such as genetic algorithm (GA) [9] and particle swarm optimization (PSO) [10], enhance robustness but are computationally demanding and prone to local optima in non-convex objectives [11]. Alternative approaches address inverse problems by constructing inverse mappings corresponding to forward problems [12], [13], [14]. The complexity of these forward problems and human factors contribute to the challenges of establishing accurate inverse mappings.

In order to overcome the limitations of traditional methods, an increasing amount of research has focused on utilizing machine learning techniques to address inverse problems. The main approach involves learning features and patterns from extensive data, which allows for the capture of complex nonlinear inverse mapping relationships. Particularly, deep learning (DL)

has provided possibilities to efficiently solve inverse problems by leveraging data-driven neural networks to model nonlinear inverse mapping functions [15], [16]. As for SAR images' view angle inversion, Guo *et al.* [17] showed that the azimuth angle prediction error varies between 13° and 33° with a DL method. Song *et al.* [18] used angle inversion accuracy as an evaluation index to measure the effect of the generated model. Due to the costly and intricate characteristics of obtaining SAR images, coupled with a scarcity of publicly accessible SAR datasets, training on limited data could not adequately capture the vast variations and specific diversities to different targets and random viewpoints [19]. Additionally, the inverse mapping relationship established by the network does not directly utilize the actual physical process of electromagnetic scattering. Such constraints result in poor performance of learning-based networks particularly when handling unseen data [20], [21], [22].

Deep reinforcement learning (DRL) has recently been recognized as a potent strategy for addressing inverse optimization problems [23], [24], [25]. DRL combines the perceptive ability of DL and the decision-making ability of reinforcement learning (RL) within interactive environments to establish the optimal policy by applying a Markov decision process and the Bellman equation [26]. Specifically, DRL guides the learning of the agent to make intelligent decisions in interactive environments by employing reinforcement signals (rewards or penalties) as feedback [27]. In comparison to traditional supervised learning methods that require massive labeled data, DRL can rely less on pre-provided strong label data to autonomously learn through interaction with the environment. Combining the ability of perceptive and decision-making allows DRL to show strong performance for complex problems, enabling learning and adaptation across different tasks [26], [28]. Moreover, the interactive learning mode of reinforcement learning makes it a great advantage in processing cross-domain data

In the field of SAR, DRL exhibits characteristics like general artificial intelligence by employing a strong interpretability policy of interactive exploration and learning, which are optimized using feedback from the environment [29], [30], [31]. For example, Xu *et al.* [30] presented the reinforcement learning and hyperband (RLH) to dynamically learn hyperparameters for ship detection from SAR images. Martin *et al.* [31] developed a method to effectively adapt the baseline of an SAR based on DRL in distributed Earth observation missions. In addition, DRL fully utilizes temporal correlations to address optimization problems of arbitrary dimensions. However, these works only focus on a few tasks, without including the SAR imaging inverse problem. How to train human-like agents capturing global discriminative and local detailed features in SAR images to interactively address radar view angle inversion problems in cases of limited data with strong cross-domain distribution backgrounds is an interesting topic, which, unfortunately, still remains largely unknown.

In this work, we introduce a DRL-based framework for training agents to interpret electromagnetic phenomena in the physical world via an electromagnetic simulator. This approach enhances the physical interpretability of solving

inverse problems. As depicted in Fig. 1, the trained agents employ strategies to progressively refine their predictions from large to small amplitude angles, converging on the true angle. Initially, we integrate a differentiable SAR render (DSR) — an embedded electromagnetic simulator — to generate SAR images at various viewing angles dynamically. This interaction between agents and DSR is pivotal in mimicking the human predictive process of angles, facilitating a continuous, adaptive learning cycle.

Further, the agents' state space is constructed using differential features in sequential and semantic aspects of angle-correlated images, which empowers the agents with an enhanced understanding of temporal context. A pre-defined discrete action space with variable step lengths is also implemented, enabling efficient and dynamic exploration and decision-making within the solution space. Finally, our reward function amalgamates several mechanisms including memory difference, smoothing, boundary penalty, and initialization noise suppression, to effectively steer the agents' learning trajectory towards achieving accurate angle prediction.

The contributions of this paper are as follows:

- We present a DRL-based inversion algorithm and first introduce an electromagnetic simulator embedded in the environment that interacts with the agent to simulate the human-like process of angle prediction. To our knowledge, it is the first DRL-based approach that emulates human-like behavior for solving view angle inversion problems in the SAR domain.
- In DRL, the state space is built using variations in features of angle-corresponding images, reducing background complexity and increasing sensitivity to time-related changes. The reward function is designed with techniques like reward memory difference and smoothing, noise suppression, and boundary penalties to improve the stability and efficiency of the inversion process.
- Extensive experimental results demonstrate the remarkable effectiveness and robustness of our proposed method in accurately predicting viewing angles of SAR images. When utilized in the cross-domain area, the proposed method significantly mitigates inconsistency between simulated and real domains.

The remainder of this article is organized as follows. Section II reviews the DSR imaging. Section III introduce the proposed method in detail. Section IV reports the experimental results. And finally, we conclude our work in Section V.

II. DSR IMAGING

SAR electromagnetic simulators are widely employed to generate SAR images by simulating various environments, providing an effective method for addressing real-world challenges and mitigating the limitations of scarce SAR observational data. Traditional coherent echo simulation methods typically established coherent models for scatterers or computed the radar cross section (RCS) of large complex targets against rough backgrounds, as referenced in [32], [33], [34]. In contrast, for non-coherent simulators, Fu *et al.* introduced

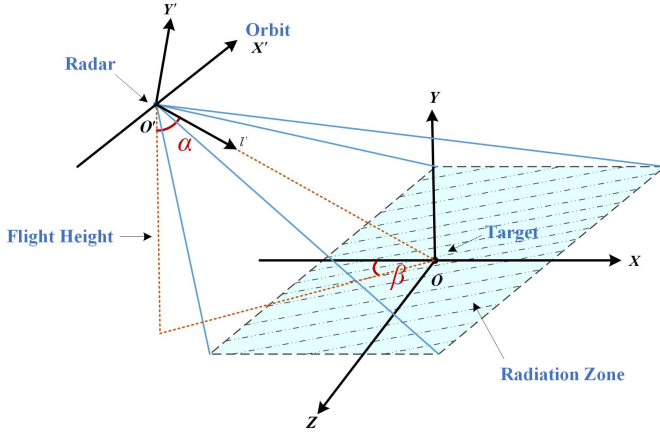


Fig. 2. SAR imaging geometric model. Related world coordinate system $O-XYZ$ and the radar coordinate system $O'-X'Y'Z'$ are defined. Our objective is to reverse the incidence angle α and azimuth angle β of radar in $O'-X'Y'Z'$.

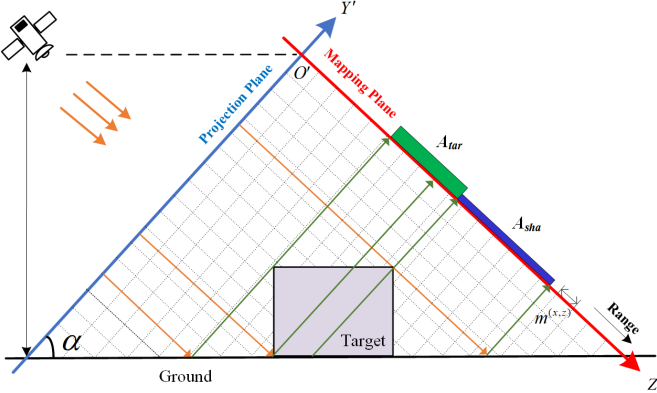


Fig. 3. The mapping and projection algorithm.

the Differentiable SAR Renderer (DSR) [35], utilizing computational graphics principles to render SAR images from 3D models to 2D projections [32].

DSR, compared to its traditional counterparts, provides several advantages including user-friendly interfacing, flexible operation, and rapid rendering capabilities. To enhance the agent's capability in exploring inherent inversion strategies, DSR has been employed in our research to render targets from arbitrary viewpoints.

A. Radar Coordinate System Definition

In SAR imaging, the vertex coordinates of the 3D mesh shape \mathcal{S} from the world coordinate system need to be converted to the radar coordinate system representation \mathcal{S}' .

As illustrated in Fig. 2, the world coordinate system is denoted as $O-XYZ$. In $O-XYZ$, the geometric target resides at point O and the radar antenna's position is A_p , which is also represented as O' . Given that the radar's azimuth orientation is $O'X'$ and its slant range direction aligns with $O'Z'$, the third axis can be deduced as $O'Y'$. Consequently, the radar coordination system is defined as $O'-X'Y'Z'$, where the incidence angle α refers to the angle between OO' and the vertical direction of the radar. The azimuth angle β is defined

as the angle between OO' and the reference direction. The range of α is $[-90^\circ, 90^\circ]$, while the range of β is $[0^\circ, 360^\circ]$. The radiation zone is the imaging area corresponding to the precise SAR image which is determined by parameters such as the target, the flight height and the radar perspectives (α, β) .

Then, the rotation matrix R is constructed to perform coordinate transformation from \mathcal{S} to \mathcal{S}' based on the defined geometric model. Specifically, the vertex set v_r in \mathcal{S}' is transformed from the vertex set v in \mathcal{S} , which can be expressed as:

$$R = \begin{bmatrix} -\cos \beta & -\cos \alpha \sin \beta & -\sin \alpha \sin \beta \\ 0 & \sin \alpha & -\cos \alpha \\ \sin \beta & -\cos \alpha \cos \beta & -\sin \alpha \cos \beta \end{bmatrix}, \quad (1)$$

$$v_r = R^T(v - A_p). \quad (2)$$

B. Imaging Mechanism

The imaging mechanism in DSR is a differentiable mapping projection algorithm [32], [35], which contains two steps: mapping and projection. As shown in Fig. 3, the imaging process is a slant-range imaging algorithm in the far field, yielding SAR images with a target area A_{tar} and a shadow area A_{sha} . The red represents the mapping plane, parallel to the range direction; the blue signifies the projection plane, perpendicular to the mapping plane, with $O'X'$ as the azimuth direction. Given the view angles (α, β) , assuming that the mapping plane contains N_m mapping units, the projection plane contains N_p projection units, and their corresponding relationship is shown in 3:

$$N_p = N_m * \tan(\alpha). \quad (3)$$

During projection, projection units on the projection plane emit multiple rays that intersect with facets of the target in space. After striking the target, the rays scatter backward and reach the mapping plane. In this way, the target's attributes from a 3D spatial are rendered onto a 2D image plane and form the A_{tar} . The accumulated backscattering intensity $I_{sar}^{(x,z)}$ of the target in the mapping unit $m^{(x,z)}$ is represented as 4.

$$I_{sar}^{(x,z)} = \sum_{n=1}^{N_f} \delta_n^{(x,z)} \cdot \omega_n^{(x,z)} \cdot S_n, \quad (4)$$

where $I_{sar}^{(x,z)}$ represents the intensity of the mapping unit $m^{(x,z)}$, N_f is the total number of target's grid facets, $\delta_n^{(x,z)}$ denotes the probability of the radar beam intersecting with facet f_n , $\omega_n^{(x,z)}$ is the ray intensity of f_n on $m^{(x,z)}$, and S_n signifies the scattering intensity of f_n .

The areas not illuminated by radar signals form the shadow region, denoted as A_{sha} . The upper boundary of A_{sha} corresponds to the lower boundary of the aforementioned target area A_{tar} , while the lower boundary of A_{sha} is determined by the mapping of the boundary beam emitted from the projection plane onto the slant range.

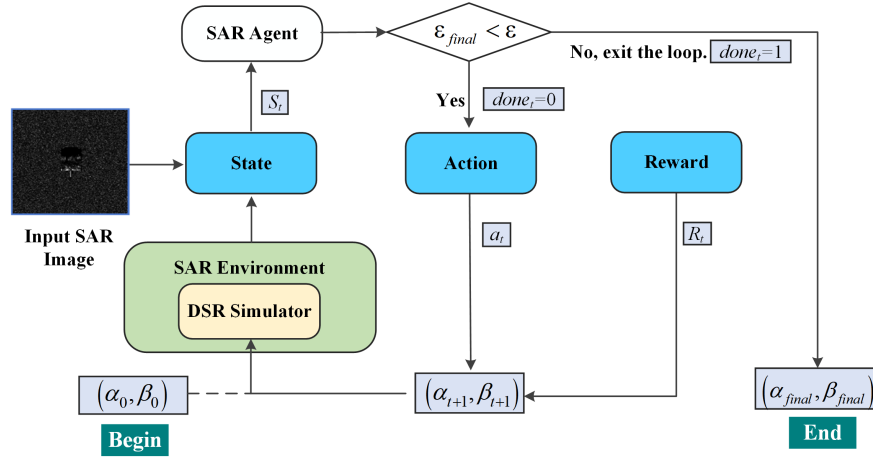


Fig. 4. The workflow of our proposed view angle inversion algorithm. The DSR embedded SAR environment generates a simulated image using a given view angle (α_t, β_t) at time t . A state representation s_t is constructed by the state construction module based on input SAR image and the simulated image. Then, upon receiving the state s_t , the SAR agent outputs two incremental angles $(\Delta\alpha_t, \Delta\beta_t)$ as an action, which are used to update the currently predicted view angles to $(\alpha_t + \Delta\alpha_t, \beta_t + \Delta\beta_t)$ to form $(\alpha_{t+1}, \beta_{t+1})$. Meanwhile, the reward construction module returns R_t to the agent in proportion to the accuracy of the inversion after the action is executed. The newly generated angles $(\alpha_{t+1}, \beta_{t+1})$ are again entered into the SAR environment for the next round of cycles.

III. METHODOLOGY

In this section, we first give an overview of the whole framework. Then the SAR environment and agent are described in detail, followed by an introduction of the DRL interactive components, including the action space, state space and reward function. Finally, we represent the training scheme of the DRL algorithm.

A. Overview

Fig. 4 depicts the workflow of the proposed inversion algorithm. When given an input SAR image, incident angle and azimuth angle (α_t, β_t) at time t , the view angle inversion begins by generating a simulated image rendered by a DSR simulator in the SAR environment. The state construction module creates the state representation s_t based on the input SAR image and the rendered image. Then, upon receiving the state s_t , the SAR agent outputs two incremental angles $(\Delta\alpha_t, \Delta\beta_t)$ as an action, which are used to update the currently predicted view angles to $(\alpha_t + \Delta\alpha_t, \beta_t + \Delta\beta_t)$ to form $(\alpha_{t+1}, \beta_{t+1})$. Meanwhile, the reward construction module returns R_t to the agent in proportion to the accuracy of the inversion after the action is executed. The newly generated angles of incidence and azimuth are again entered into the SAR environment for the next round of cycles. The initial incident angle and azimuth angle (α_0, β_0) at time $t = 0$ are random sampled from predefined distributions. Following the above process, the inversion task continues until the predefined termination condition is met.

We delineate in Fig. 5 the comprehensive architecture of the proposed framework, encompassing various DRL modules such as the SAR environment and agent, action space, state space, and reward function. The SAR environment integrates a SAR simulator, denoted as DSR, to facilitate the generation of SAR images, thereby aiding in the emulation of human-like angle prediction. The agent is crafted using the Dueling DQN

architecture, enabling it to yield incremental adjustments to the angles in the defined action space.

The action module is designed with six discrete adjustments for each angle to quantitatively modify predicting view angles. The state module employs SARNet, a feature extraction network, to construct the state by capitalizing on the differences in sequential and semantic features across angle-corresponding images. This approach is instrumental in diminishing the impact of complex backgrounds and amplifying sensitivity to temporal changes and local nuances. The reward module is an amalgamation of various mechanisms: reward memory difference, reward smoothing, initialization noise suppression, and boundary penalties. This confluence of strategies is aimed at bolstering the stability and expediting the convergence of the inversion process.

Subsequent sections will elaborate on the specific design elements and functional intricacies of these DRL modules.

B. SAR Environment and Agent

1) *DSR Embedded SAR Environment*: The method proposed in this paper embeds DSR in the interactive environment of the agent, facilitating iterative learning for the agent. By altering the observation perspective, different SAR images can be generated by DSR. When interacting with the agent, DSR renders arbitrary view target SAR images in real-time to promote the human-like angle prediction process, improving the agent's interactive perception and understanding of the target observation Angle. Fig. 6 (a) shows the 3D shape of the T62. And Fig. 6 (b) shows the DSR-rendered SAR images with a textured T62 model. The rows represent different incident angles, and the columns represent different azimuth angles.

2) *SAR Agent*: The SAR agent is composed of two networks: the action value network and the target action value network. These networks fulfill the role of estimating Q-values associated with each action within a given state and calculating the target Q-values during the learning process to subsequently

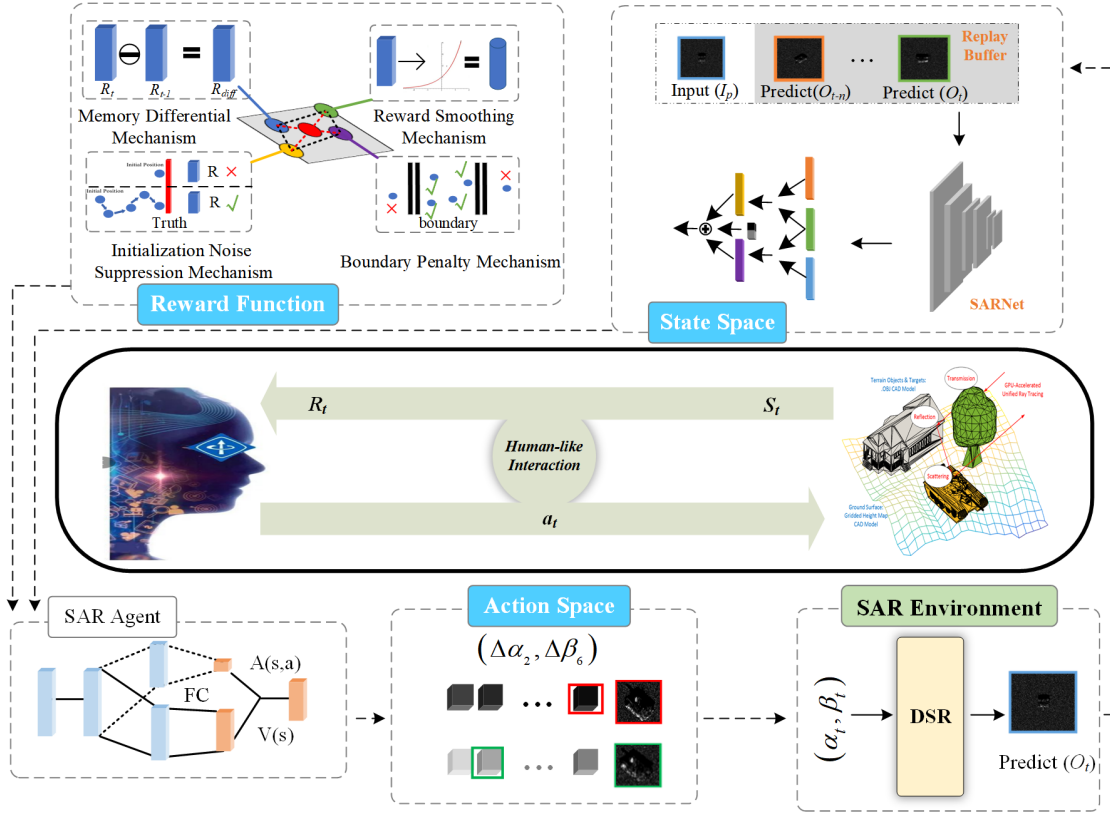


Fig. 5. The overall architecture of our proposed framework and the details of the different DRL modules including the SAR environment and agent, action space, state space and reward function. The reward R_t is obtained to evaluate the inversion effect at time t . The option chosen by the agent depends on the currently learned policy.

update the parameters of the action value network. Both networks adhere to the architecture in the Rainbow algorithm [36]. The network ultimately produces a probability distribution encompassing various potential actions, contributing to the training trajectory of the agent.

C. DRL Interactive Components

We formulate the inverse problem of radar perspectives as a Markov decision process to discover the optimum strategy by maximizing the cumulative rewards obtained during interactive episodes. The details of the Markov decision process are designed as follows:

- Action space: A is the set of actions, representing the incremental angles a_t for current view angles at time t .
- State space: S is the set of states, representing the state s_t generated at time t from the observation I_t .
- Reward function: R is the reward function, representing the reward R_t obtained by executing action a_t in s_t at time t .

1) *Action Space*: At time t , the action a_t is defined as the step $(\Delta\alpha_t, \Delta\beta_t)$ to adjust the current view angles (α_t, β_t) quantitatively. Actions are categorized into three subsets, representing different degrees of discrete adjustments for manipulating view angles during interaction with the environment. For each level of adjustment, given the distinct ranges of α and β , separate controls α_i and β_i are employed for angle movement. This arrangement enables the agent to adopt an

exploratory strategy with larger movements initially and a refined exploitation strategy later, enhancing the speed of inversion. Additionally, a terminal action $(0, 0)$ is introduced to terminate the inversion process and ensure policy stability. Then a_t is as follows:

$$a_t = \{(x, y) | x \in \{\pm\alpha_i, 0\}, y \in \{\pm\beta_i, 0\}\}, i \in [1, 2, 3], \quad (5)$$

where α_i, β_i are hyper-parameters. The hyper-parameters selected are relevant to the maximum steps in each episode, which enables the agent to search and make decisions in the solution space effectively and gives a good trade-off between inversion accuracy and speed.

2) *State Space*: We employ SARNet, a feature extraction network, as a global discriminative feature extractor to capture high-level semantic and low-level spatial information in SAR images, thereby facilitating precise view angle reasoning. SARNet, structured on the ResNet framework, integrates convolutional layers, residual connections, batch normalization, and non-linear activation functions as its foundational modules. These modules collectively enhance incremental feature learning. As a result, the compounded depth and complexity of SARNet significantly improve its capabilities in feature extraction and classification.

The construction of the state space is crucial, providing the agent with comprehensive temporal information and enhancing algorithmic robustness. We define the observation at time t as a tuple $o_t = (I_p, S(\alpha_t, \beta_t), (\alpha_t, \beta_t))$, where I_p denotes

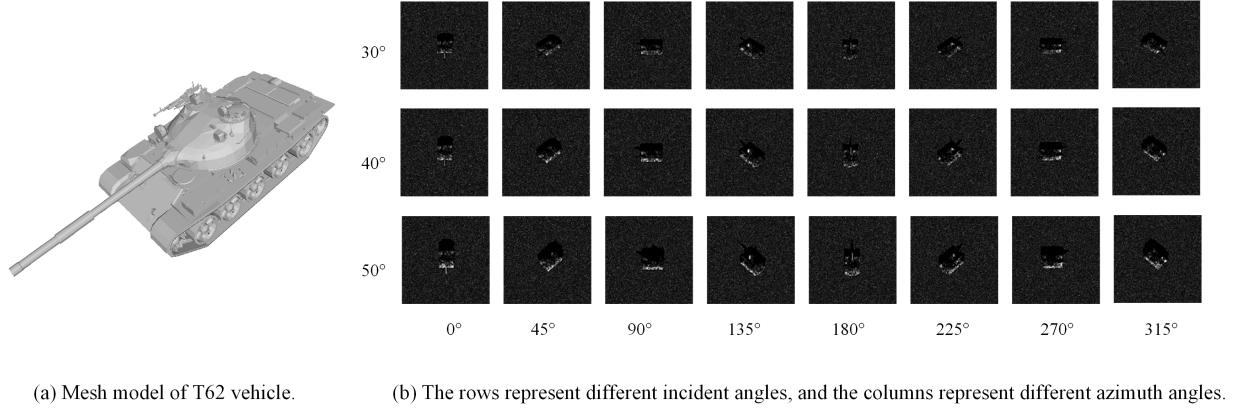


Fig. 6. DSR-rendered simulated SAR images with textured T62 model at different angles.

the input image, (α_t, β_t) the current predicted view angles, and $S(\alpha_t, \beta_t)$ the rendered image for angles (α_t, β_t) . The state space is constructed from the differential features of sequential and semantic attributes among consecutive rendered images. Specifically, it comprises the feature differential between $S(\alpha_{t-1}, \beta_{t-1})$ and $S(\alpha_t, \beta_t)$ for temporal variation, and between $S(\alpha_t, \beta_t)$ and I_p to discern semantic changes and trajectory shifts due to variations in predicted view angles. Inclusion of the current estimated view angles (α_t, β_t) as the final part offers direct guidance for policy updates, aligning with the agent's objective of accurately estimating target view angles in the SAR image. The state space is represented in the following way:

$$s_t = \left(\begin{array}{c} F(S(\alpha_t, \beta_t)) - F(S(\alpha_{t-1}, \beta_{t-1})), \\ F(S(\alpha_t, \beta_t)) - F(I_p), (\alpha_t, \beta_t) \end{array} \right), \quad (6)$$

where S denotes electromagnetic simulator, F denotes pre-trained feature extraction network. By learning the prior knowledge contained in the training SAR images, SARNet captures the robust scattering and morphological features of the target under different view angles from input SAR images.

3) *Reward Function*: The reward function R_t is pivotal in our inversion task, enabling the agent to iteratively refine its policy based on state s_t and corresponding actions. It comprises four components: $R_{\text{base}}^t, R_1^t, R_2^t, R_3^t$. Subsequent sections delineate the design principles of these components.

Initially, we construct the reward r_1^t for each angle θ by quantifying the discrepancy between the inversion outcome and the actual angle. This metric motivates the agent to adjust its actions toward the accurate angle, granting a minor negative reward for proximity and a more substantial negative reward as the deviation increases

$$r_1^t(\theta) = -L_1(\theta_t, \theta_r), \quad (7)$$

$$r_{1'}^t(\theta) = -L_1(\theta_t, \theta_0). \quad (8)$$

To expedite the convergence of the inverse policy, we have formulated R_{base}^t as shown in (9). R_{base}^t employs a reward memory differential approach to encapsulate the sequential disparity between r_1^t and r_1^{t-1} , directly steering the agent's

parameter optimization. Specifically, a decrease in R_{base}^t indicates an action leading away from the objective, suggesting the agent is diverging from the optimal path. Conversely, a positive R_{base}^t signals alignment with the correct inversion trajectory, prompting continued exploration in that vector

$$R_{\text{base}}^t = r_1^t(\theta) - r_1^{t-1}(\theta). \quad (9)$$

To mitigate the inversion process's instability, potentially causing erratic policy performance, we introduce a negative exponential reward r_2 . This strategy ensures smooth, gradual adjustments towards the target value and discourages abrupt, unstable actions. Moreover, to avert the agent's fixation on optimizing a solitary parameter, we have structured the reward function to foster simultaneous optimization of multiple parameters, specifically α and β , with distinct parameters $\eta_1 = -0.05$ and $\eta_2 = -0.2$ respectively

$$r_2(o|\eta) = \exp(\eta \cdot o), \quad (10)$$

$$R_1^t = r_2(r_1^t(\theta)|\eta). \quad (11)$$

In cases where initial view angles are suboptimal, the replay mechanism's efficiency diminishes, leading to reward fluctuations within an episode. Notably, when starting near the true value, relying solely on R_1^t diminishes exploration, risking convergence to local optima. To counteract the variability from initial conditions, an auxiliary reward, R_2^t , is introduced as indicated in (12).

$$R_2^t = 5 \sum_{i=1}^3 A(\alpha|\rho_i, \varphi_i) \cdot A(\beta|\nu_i, \omega_i), \quad (12)$$

$$s.t. A(\theta|\kappa_i, \varsigma_i) = \begin{cases} 1 & \text{if } |r_1^t(\theta)| < \rho_i \ \& \ |r_1^{t'}(\theta)| > \varphi_i, \\ 0 & \text{otherwise,} \end{cases}$$

where $\rho_i, \varphi_i, \nu_i, \omega_i$ are hyper-parameters. Here, $A(\theta|\kappa_i, \varsigma_i)$ activates only when precise conditions of proximity and improvement are met, encouraging comprehensive optimization and escalating rewards as the challenge of adjustment intensifies. This mechanism averts scenarios of substantial rewards for minimal or no actual improvement.

To deter the agent from straying beyond the beneficial parameter space, thereby disrupting the exploration continuum, we impose a penalty through R_3^t . Set to -10 , this punitive measure bounds the action outputs, fostering a focused, effective exploration within the permissible parameter range

$$R_t = R_{\text{base}}^t + R_1^t + R_2^t + R_3^t. \quad (13)$$

The intricate composition of R_t effectively amalgamates individual rewards, counteracting policy non-convergence issues common in sparse reward scenarios in RL. It ensures methodical, quality actions at each iteration, enhancing the learning trajectory and propelling the agent towards peak performance.

D. Training Scheme of the DRL Algorithm

Our objective is to infer the radar view angles $[\alpha, \beta]$ inherent to the SAR image X , utilizing Deep Reinforcement Learning (DRL) to learn the mapping policy $F_{\Theta} : X \rightarrow [\alpha, \beta]$. Given the discrete nature of the action space, the Rainbow algorithm [36] is employed for its compatibility with discrete actions [28] and its enhancement of learning efficiency and training stability.

We initialize the action value network $Q(s, a|\theta)$ parameters as θ and the target action value network $Q'(s, a|\theta')$ parameters as θ' . The agent then proceeds with iterative interactions across multiple episodes. In each episode, the Q-network receives state s_t and outputs probabilities for various actions. It follows an ϵ -greedy strategy, exploring with probability ϵ and exploiting with $1 - \epsilon$. Over time, this strategy is refined by linearly decreasing ϵ , incrementally favoring exploitation. Interactions terminate upon reaching the environment's maximum step count, signaling a terminal state. Each episode's trajectories are stored in an experience replay buffer, adopting a prioritized strategy from the Rainbow algorithm for efficient learning by extracting high-priority samples based on their estimated value. The parameter update for the Q-network, influenced by a discount factor γ , is formalized in (14)

$$loss = \left(\frac{R_t + \gamma Q_{\theta'} \left(s_{t+1}, \underset{a'}{\operatorname{argmax}} Q_{\theta} (s_{t+1}, a') \right) - Q_{\theta} (s_t, a_t)}{Q_{\theta} (s_t, a_t)} \right)^2. \quad (14)$$

Throughout the testing phase, the refined network parameters are directly employed to yield precise probability estimates for all possible action executions corresponding to a provided state. After several iterations, the final inversion angles can be gained.

IV. EXPERIMENTS

In this section, we introduce the experimental setup and the implementation details of agent training and testing. Furthermore, we undertake a thorough assessment of our proposed algorithm, encompassing extensive quantitative experiments, evaluation of action strategy, ablation analyses and domain adaptation experiments.

A. Experimental Dataset

1) *Simulated Dataset*: In this study, simulated SAR images for training and testing are synthesized using DSR rendering. According to the incident angle criteria defined herein, surpassing a certain threshold causes the target's projected position to extend outside the image bounds, leading to loss of critical target configuration and contour data. This impacts the agent's ability to develop a consistent inversion strategy. To maintain image fidelity, the agent's view angles are set within a range of incidence angles $[30^\circ, 75^\circ]$ and azimuth angles $[0^\circ, 359^\circ]$. All rendered images are standardized to a resolution of 128×128 pixels.

2) *Real Dataset*: The MSTAR dataset is utilized to validate the generalization ability of the proposed algorithm [37]. It encompasses various vehicle types imaged at multiple viewing angles. The images are captured in spotlight mode with a resolution of $0.3\text{m} \times 0.3\text{m}$ and formatted into 128×128 pixel chips. Azimuth angles span from 0 to 360° at approximately $1\text{-}2^\circ$ intervals. The dataset includes depression angles of 17° and 15° .

B. Experiment Setup

1) *Experiment Model*: This study selects T62 as a 3D model and employs DSR rendering this shape to validate the efficacy of our algorithm.

Due to varying scattering characteristics of objects and observation conditions, the imaging results for the same target also differ. To generate realistic simulated SAR images, the standard gamma distributions are used to extract scattering textures of objects in the MSTAR dataset [37]. Firstly, the SAR image is segmented into the target region and background region with the segment anything algorithm [38]. Next, gamma distributions are independently fitted to the texture attributes of these two distinct regions (see Fig. 7), and the parameters of the two distributions are tabulated within Table I. The values obtained through stochastic sampling from the above distributions are then designated as textures attributed to the surface of the 3D target and the ground and hence a 3D model enriched with scattering textures is obtained.

2) *Experiment Configuration*: All network models discussed in this article are implemented using PyTorch, a Python-based DL framework. The training and testing of these models are conducted on an NVIDIA GeForce RTX 2080 Ti graphics card, utilizing CUDA 10.1 and cuDNN 8.0.5 for accelerated computations. During the training phase, the model parameters are optimized using the Adam optimization algorithm [8]. In the RL framework, the capacity of the replay buffer is 50,000, allowing the agent to store data until the buffer is full. Both agent networks are trained with a batch size of 256 and a learning rate of $1e - 5$. To facilitate exploration, an ϵ -greedy strategy is employed, and ϵ is linearly annealed from 0.5 to 0.01 according to this policy. The discount factor γ is set to 0.96, and the target network is updated every 200 steps.

The feature extraction network is trained on DSR-rendered simulated SAR data generated by uniform sampling within pre-defined angle distribution regions, which ensures that the

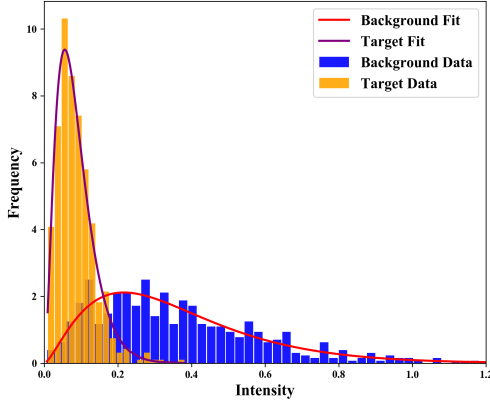


Fig. 7. Gamma Distribution Fitting.

generated samples encompass a variety of real-world SAR scenarios. Two distributions are formulated as:

$$D_\alpha \sim D_{\text{uniform}}(a, b | \rho), a = 35, b = 75, \rho = 5, \quad (15)$$

$$D_\beta \sim D_{\text{uniform}}(c, d | \nu), c = 0, d = 360, \nu = 5, \quad (16)$$

where a, b are the starting and ending angles of distribution D_α respectively, ρ denotes the sampling interval. The parameter definition of distribution D_β is as same as distribution D_α .

3) *Evaluation Metrics*: To assess the angle inversion performance of the agent, we employ kinds of metrics such as *MAE*, *MAPE*, *RMSE* and *MedAE*. Denote by \tilde{P}^i and P^i the inversion estimated and the true angles for the i_{th} sample, respectively. Denote by n the total number of samples.

- *MAE* assesses the disparity between predicted values and actual observations and assigns equal weight to all samples, which evaluates the fundamental performance of our model

$$MAE = \frac{1}{n} \sum_{i=1}^n |\tilde{P}^i - P^i|. \quad (17)$$

- *MAPE* calculates the average percentage error of predicted values relative to the actual observations, which emphasizes the assessment of predictive performance where true values exhibit significant variations

$$MAPE = \frac{1}{n} \sum_{i=1}^n \left| \frac{P^i - \tilde{P}^i}{P^i} \right|. \quad (18)$$

- *RMSE* measures the average size of the agent's prediction error in the form of root-mean-square, which primarily evaluates the generalization ability of our model for outliers

$$RMSE = \sqrt{\frac{1}{n} \sum_{i=1}^n (P^i - \tilde{P}^i)^2}. \quad (19)$$

TABLE I
PARAMETERS OF THE GAMMA DISTRIBUTIONS.

Region	Shape Parameters	Scale Parameters
Target	2.311	0.162
Background	2.867	0.029

- *MedAE* quantifies the median absolute difference between actual observations and their corresponding predictions, which concentrates on the accuracy of predictions for inliers

$$MedAE = \text{median}(|\tilde{P}^i - P^i|). \quad (20)$$

C. Inversion Strategy Evaluation

This segment presents reward curves that illustrate the progression observed during the training phase of the proposed algorithm. In addition, the performance of the agent in the testing phase is also validated.

1) *Comparative experiments*: In order to further verify the performance of our proposed algorithm, we compare it with the GA algorithm, PSO algorithm, DL algorithm and DL combined with the DRL algorithm. The basic idea of GA and PSO algorithms is to model the view angles inversion problem as an optimization problem. Its objective is to minimize the difference between the input image and the rendered image associated with inverse angles, which is equal to finding the minimum of the objective function. To accelerate the optimization process and enhance its precision, the fitness functions of the two algorithms are designed as the feature difference between two images as (21):

$$J(\alpha, \beta) = \|F(S(\alpha, \beta)) - F(S(\alpha_p, \beta_p))\|_1. \quad (21)$$

In contrast to the mechanism of the above optimization algorithms, the DL algorithm aims to employ neural networks to fit the inverse mapping function of our task. Then a dataset consisting of 576 DSR-rendered T62 target SAR images is created, encompassing α within $[35^\circ, 70^\circ]$ in 5-degree intervals and β within $[0^\circ, 360^\circ]$ in 5-degree intervals. The DL network structure aligns with the previously mentioned pre-trained model network structure.

Several researchers have adopted an integrated methodology that merges DL and DRL. In this amalgamation, RL is applied to enhance DL models meticulously, exemplified by systems like ChatGPT, which function within an RL paradigm augmented by human feedback. This approach stems from the recognition that DL primarily focuses on generating complex mappings without sufficiently addressing the underlying optimization strategies. Furthermore, the limited interpretability and robustness of DL pose significant challenges in integrating physical priors into models. Conversely, relying exclusively on RL agents to navigate the solution space proves to be an extensive process. Consequently, this paper contrasts the DRL algorithm with the combined DL and DRL strategy. Specifically, it utilizes DL-derived outputs as the initial states for DRL, refining these outputs to align the agent's initial

TABLE II
METRICS COMPARISON RESULTS OF DIFFERENT ALGORITHMS ON DSR-RENDERED SAR IMAGES. THE BEST RESULT FOR EACH METRIC IS HIGHLIGHTED IN BOLD.

Method	MAE_{α}	MAE_{β}	MAE_{mean}	$MAPE$	$RMSE$	$MedAE$	Run Time (s)
GA[9]	4.580	8.612	6.596	0.086	7.489	5.892	115.600
PSO[10]	6.249	11.416	8.833	0.118	9.890	3.797	58.912
DL[39]	2.052	3.993	3.023	0.040	3.578	2.078	0.160
DRL (Ours)	1.594	3.797	2.696	0.043	3.168	2.000	2.282
DL+DRL (Ours)	1.282	1.960	1.621	0.030	2.070	1.239	0.508

TABLE III
METRICS COMPARISON RESULTS OF DIFFERENT ALGORITHMS ON MSTAR. THE BEST RESULT FOR EACH METRIC IS HIGHLIGHTED IN BOLD.

Method	MAE_{α}	MAE_{β}	MAE_{mean}	$MAPE$	$RMSE$	$MedAE$	Run Time (s)
GA[9]	8.353	15.574	11.963	0.109	13.551	9.016	94.639
PSO[10]	5.306	12.396	8.851	0.086	10.464	4.399	106.667
DL[39]	1.359	6.859	4.109	0.037	5.087	1.499	0.157
DRL (Ours)	1.282	6.169	3.726	0.033	4.403	2.895	1.350
DL+DRL (Ours)	1.099	5.618	3.359	0.034	4.163	2.479	1.049

estimates more closely with the actual solution, thus reducing the time required for exploration.

Table II presents a comparative analysis of the mean inversion performance, considering the accuracy and time consumption. The best result for each metric is highlighted in bold. In terms of accuracy, the DRL method outperforms both optimization algorithms and DL methods, yielding the smallest error in MAE_{α} , MAE_{β} , MAE , $RMSE$ and $MedAE$, where MAE represents the average inversion error of two angles. Compared to the DL method, a reduction of 0.327, 0.410 and 0.078 on MAE , $RMSE$ and $MedAE$ can be achieved by our DRL method. The MAE and $RMSE$ of DRL are merely 2.696 and 3.168 degrees, showcasing a significant advantage on all samples and outliers. This outcome substantiates the higher precision of the DRL inversion algorithm, primarily attributable to the well-designed s_t in RL that captures the physical features and semantic information of SAR images, effectively harnessing temporal information as well. Compared to the DL and DRL methods, our DL+DRL method gets state of the art in MAE_{α} , MAE_{β} , MAE , $RMSE$ and $MedAE$ metrics. The results demonstrate that our DL+DRL method uses the robust feature extraction of DL and the strategic decision-making ability of RL. This synergy offers a more effective method for addressing complex, dynamic problems requiring long-term planning and strategy formulation. Regarding the processing speed of models, the combination of DL and DRL requires only 10 interaction steps to achieve a more accurate inversion result. This is due to the swift convergence achieved by replacing random initialization with DL-predicted angles, thus localizing the solution near optimality, coupled with a finer granularity in the action space settings.

2) *Domain Adaptation*: Discrepancies between SAR simulators and practical radar sensors create significant domain gaps between simulated and real data, often yielding suboptimal model performance with real-world data. Nevertheless, the DRL interaction framework demonstrates robust generalization capabilities across domains. Notably, by fine-tuning with a minimal set of target domain samples, the agent effectively explores similarities between the training and target domains through interaction, thereby acquiring adaptive cross-domain policies. To empirically validate the generalization of our proposed framework, a subset of real T62 category images from the MSTAR dataset [37] are integrated into the training phase. In each episode, a randomly selected real image is inputted, followed by iterations using DSR-simulated data. The fine-tuned agent is then employed to reconstruct the radar perspective of previously unseen real images.

The results of these domain adaptation experiments are delineated in Table III. The table reveals that the predicted MAE and $RMSE$ values are relatively low due to the MSTAR dataset's narrow range of incidence angles, while the azimuth angles span $[0^{\circ}, 360^{\circ}]$, augmenting prediction complexity and error margins. Despite increased deviation in measured data, the overall inversion error remains modest, underscoring the method's robustness in managing cross-domain datasets. $MedAE$, an outlier-resistant metric, shows that excluding outliers significantly enhances DL performance, thereby confirming the superior generalization of our DRL methods over conventional DL techniques in outlier scenarios.

D. Evaluation of Agent's Action Strategy

1) *Training Inversion Agent*: In order to ensure the agent's convergence, the maximum training iteration is set to 500.

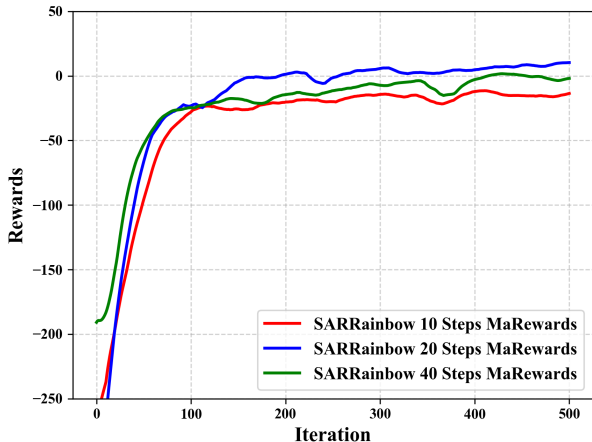


Fig. 8. Reward curves of three agents with different steps in the training phase.

When reaches the maximum, the agent concludes its training. Within an episode, termination is triggered under two circumstances: if the interaction steps attain the pre-defined maximum step in each episode, or if MAE_{angle} descends below 2 degrees. The interaction steps are assigned distinct values in each episode for different training times, specifically 10, 20 and 40 steps respectively.

The reward curves corresponding to these three agents of different interaction steps are visually presented in Fig. 8. In Fig. 8, all three curves adhere to the expected trajectory: as training progresses, the cumulative reward for each interaction quickly rises and stabilizes around the 120th iteration. In subsequent iterations, some minimal fluctuations exist attributable to the inherent randomness in the selection of initial angles. Despite these minute fluctuations, the reward curves remain relatively stable. This pattern confirms the effectiveness and robustness of our task modeling.

2) *Visualization of MAE*: We visualized the normalized average change in MAE_{angle} with increasing interaction steps during a single episode. This metric intuitively reflects the normalized discrepancy between inversion results and ground truth. As depicted in Fig. 9, as the number of interaction steps increases, the inversion results gradually converge towards the ground truth. When the average action selection number reaches around 5, the MAE converges to a relatively low value. Upon further increasing the interaction steps to approximately 15, the agent nearly achieves complete convergence.

3) *Visualization of Agent's Action Selection*: According to the design of the action space in this paper, it is evident that three sets of action adjustment parameters are established, representing three adjustment magnitudes for two angles. To investigate whether the agent has learned a phased exploration strategy, the iterative process of each episode is evenly divided into the early stage and the late stage based on the total number of steps taken by the agent. Theoretically, in the early stage, the agent tends to adopt a larger action adjustment magnitude to narrow down the solution space swiftly. In the late stage, the agent employs smaller actions for fine-tuning to enhance

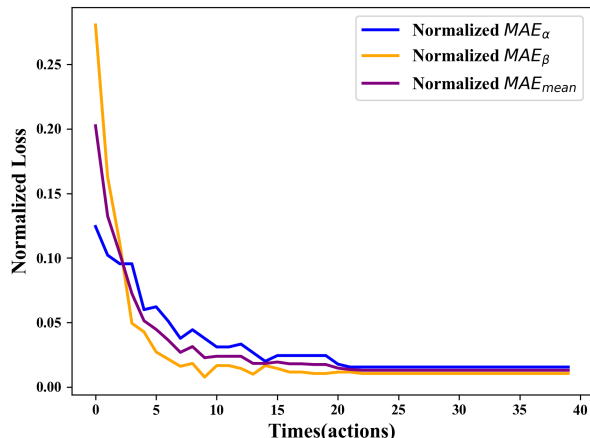


Fig. 9. Average normalized change in MAE_{angle} with increasing interaction steps during a single episode.

inversion accuracy.

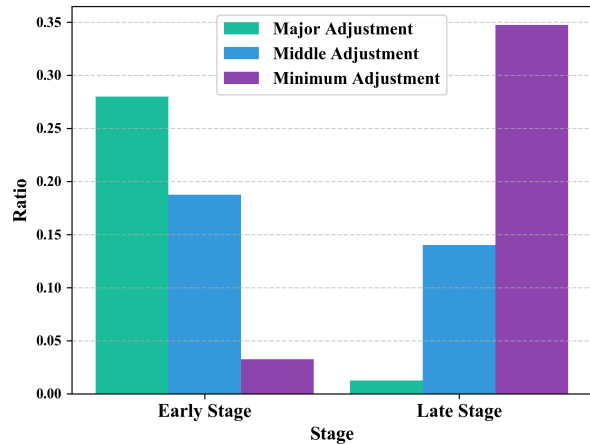


Fig. 10. Frequency for different adjustments of the actions generated by the SAR agent.

Fig. 10 visualizes this process, demonstrating that the proportion of actions corresponding to larger adjustment values is notably higher during the first stage than in the late stage. Conversely, during the late stage, there is a higher proportion of actions involving smaller adjustment values. It obviously aligns with the expected outcomes, validating that the agent can indeed learn a phased inversion strategy.

E. Ablation Study

1) *Contribution of State and Reward*: In this section, a series of ablation experiments are conducted to examine the effectiveness of s_t and R^t in our proposed RL framework. Ablation experiments present comprehensive results and comparative analysis of angle inversion outcomes, including MAE_{angle} , $MAEI_{angle}$, MAE_{mean} . We use the SD and FD to represent the temporal difference and feature difference

TABLE IV
ABLATION STUDY OF S_t AND R_t .

Model	MAE_α	MAE_β	MAE_{mean}	Outliers
Model with S_{base} and R_t	2.159	3.839	2.999	9
Model with S_t and R_{base}	2.020	4.452	3.238	5
Model with S_t and R_t	1.578	3.662	2.620	4

TABLE V
ABLATION STUDY OF S_t .

Model	MAE_α	MAE_β	MAE_{mean}	Outliers
Model with S_t -w/o SD, FD	2.125	5.458	3.792	12
Model with S_t -w/o FD	2.535	4.315	3.425	10
Model with S_t	2.020	4.452	3.236	5

modules of S_t , respectively. During the inversion process, anomalies sometimes arise during the inversion process. Thus, points with AE_{angle} exceeding 50 degrees are categorized as outliers. By monitoring the number of outliers, the agent's stability is assessed. The following table sequentially presents the quantitative results of each ablation experiment, where each set of values represents the average outcome of 1,000 experimental episodes.

As depicted in Table IV, a controlled variable approach is employed to conduct three sets of experiments. The first two rows focus on ablations pertaining to the state space and reward function, respectively. Compared with the third row, it is evident that both the state space and the reward contribute to an enhancement in the inversion accuracy of both angles, thereby reducing the count of outliers. Furthermore, subsequent ablation experiments were performed on individual submodules within the state space and the reward was to further validate their effectiveness.

2) *State Components*: When the state space submodule is ablated, the reward function used is R_{base} . Table V presented that the average inversion loss of the model gradually decreases after the sequential difference module and feature difference module are gradually added to the state representation. The addition of a sequential difference module significantly improves the inversion accuracy, and the feature difference effectively reduces the number of outliers. The quantitative results highlight that the simultaneous use of the sequential difference module and the feature module effectively ensures the accuracy of the inversion of view angles.

3) *Reward Components*: To individually explain the necessity of each submodule of R_t , the performance of the algorithm was evaluated by sequentially removing each of the three components of the reward function. After confirming the effectiveness of the state space in Table V, during the ablation of the reward, the state is fixed to S_t . Table VI presents the quantitative outcomes of various reward function configurations, which indicate that all employed reward components are effective.

V. CONCLUSION

In this study, we investigate the application of DRL to the problem of reverse engineering radar view angles in SAR images. We develop a DRL framework that mimics

TABLE VI
ABLATION STUDY OF R_t .

Model	MAE_α	MAE_β	MAE_{mean}	Outliers
Model with R_t -w/o R_1^t, R_2^t, R_3^t	3.417	4.243	3.830	5
Model with R_t -w/o R_2^t, R_3^t	2.719	4.541	3.630	8
Model with R_t -w/o R_3^t	2.570	4.575	3.573	6
Model with R_t	1.578	3.662	2.620	4

human learning processes, allowing an agent to reverse-engineer angles by interacting with an environment coupled with an electromagnetic simulator. The designed state space effectively reduces background noise, enhances sensitivity to temporal changes, and improves the ability to discern local target information. Additionally, we craft a reward function that employs a differential reward memory mechanism and initial noise reduction techniques to improve the stability and convergence of the agent's learning process. Our extensive experiments validate that the proposed DRL approach achieves a commendable balance between accuracy and efficiency and performs robustly on both simulated and real-world data.

Conclusively, we posit that our method provides a foundational step towards the utilization of RL in conjunction with electromagnetic simulators to address inverse problems in SAR imagery. Although our current efforts focus on lower-dimensional challenges, future work will extend to more complex scenarios, including the construction of three-dimensional models from SAR images via advanced DRL techniques.

REFERENCES

- [1] A. Moreira, P. Prats-Iraola, M. Younis, G. Krieger, I. Hajnsek, and K. P. Papathanassiou, "A tutorial on synthetic aperture radar," *IEEE Geoscience and remote sensing magazine*, vol. 1, no. 1, pp. 6–43, 2013.
- [2] Y. Zhou, H. Liu, F. Ma, Z. Pan, and F. Zhang, "A sidelobe-aware small ship detection network for synthetic aperture radar imagery," *IEEE Transactions on Geoscience and Remote Sensing*, vol. 61, pp. 1–16, 2023.
- [3] M. Ulrich, S. Braun, D. Köhler, D. Niederlöhner, F. Faion, C. Gläser, and H. Blume, "Improved orientation estimation and detection with hybrid object detection networks for automotive radar," in *2022 IEEE 25th International Conference on Intelligent Transportation Systems (ITSC)*. IEEE, 2022, pp. 111–117.
- [4] L. He, R. Panciera, M. A. Tanase, J. P. Walker, and Q. Qin, "Soil moisture retrieval in agricultural fields using adaptive model-based polarimetric decomposition of sar data," *IEEE Transactions on Geoscience and Remote Sensing*, vol. 54, no. 8, pp. 4445–4460, 2016.
- [5] X. Zhang and F. Xu, "Coherent spatially varying bidirectional scattering distribution function of rough surface," *IEEE Transactions on Geoscience and Remote Sensing*, vol. 60, pp. 1–17, 2021.
- [6] S. Ruder, "An overview of gradient descent optimization algorithms," *arXiv preprint arXiv:1609.04747*, 2016.
- [7] R. S. Sutton, "Two problems with backpropagation and other steepest-descent learning procedures for networks," in *Proc. of Eighth Annual Conference of the Cognitive Science Society*, 1986, pp. 823–831.
- [8] D. P. Kingma and J. Ba, "Adam: A method for stochastic optimization," *arXiv preprint arXiv:1412.6980*, 2014.
- [9] J. H. Holland, *Adaptation in natural and artificial systems: an introductory analysis with applications to biology, control, and artificial intelligence*. MIT press, 1992.
- [10] J. Kennedy and R. Eberhart, "Particle swarm optimization," in *Proceedings of ICNN'95-international conference on neural networks*, vol. 4. IEEE, 1995, pp. 1942–1948.
- [11] Z. Beheshti and S. M. H. Shamsuddin, "A review of population-based meta-heuristic algorithms," *Int. j. adv. soft comput. appl.*, vol. 5, no. 1, pp. 1–35, 2013.
- [12] O. Karakuş, I. Rizaev, and A. Achim, "Ship wake detection in sar images via sparse regularization," *arXiv preprint arXiv:1904.03309*, 2019.

- [13] J. Kallestad, R. Hasibi, A. Hemmati, and K. Sørensen, "A general deep reinforcement learning hyperheuristic framework for solving combinatorial optimization problems," *European Journal of Operational Research*, vol. 309, no. 1, pp. 446–468, 2023.
- [14] Z. Zhou, S. Wei, H. Zhang, R. Shen, M. Wang, J. Shi, and X. Zhang, "Saf-3dnet: Unsupervised amp-inspired network for 3-d mmw sar imaging and autofocusing," *IEEE Transactions on Geoscience and Remote Sensing*, vol. 60, pp. 1–15, 2022.
- [15] L. Li, Z. Zhou, S. Wu, and Y. Cao, "Multi-scale edge-guided learning for 3d reconstruction," *ACM Transactions on Multimedia Computing, Communications and Applications*, vol. 19, no. 3, pp. 1–24, 2023.
- [16] Z. Zhou, L. Li, S. Wu, X. Li, K. Ma, and X. Zhang, "Replay attention and data augmentation network for 3-d face and object reconstruction," *IEEE Transactions on Biometrics, Behavior, and Identity Science*, vol. 5, no. 3, pp. 308–320, 2023.
- [17] Q. Guo, H. Xu, and F. Xu, "Causal adversarial autoencoder for disentangled sar image representation and few-shot target recognition," *IEEE Transactions on Geoscience and Remote Sensing*, 2023.
- [18] Q. Song, F. Xu, X. X. Zhu, and Y.-Q. Jin, "Learning to generate sar images with adversarial autoencoder," *IEEE Transactions on Geoscience and Remote Sensing*, vol. 60, pp. 1–15, 2021.
- [19] Q. Guo and F. Xu, "Learning low-dimensional sar target representations from few samples," in *2022 International Applied Computational Electromagnetics Society Symposium (ACES-China)*. IEEE, 2022, pp. 1–2.
- [20] X. Feng, W. Haipeng, and J. Yaqiu, "Deep learning as applied in sar target recognition and terrain classification," *Journal of Radars*, vol. 6, no. 2, pp. 136–148, 2017.
- [21] X. X. Zhu, D. Tuia, L. Mou, G.-S. Xia, L. Zhang, F. Xu, and F. Fraundorfer, "Deep learning in remote sensing: A comprehensive review and list of resources," *IEEE geoscience and remote sensing magazine*, vol. 5, no. 4, pp. 8–36, 2017.
- [22] Q. Guo, Y. Qian, H. Wang, W. Yu, F. Xu, T. J. Cui, and Y.-Q. Jin, "Recognition rate versus substitution rate curve: An objective utility assessment criterion of simulated training data," *IEEE Transactions on Geoscience and Remote Sensing*, vol. 60, pp. 1–15, 2022.
- [23] B. Sridharan, S. Mehta, Y. Pathak, and U. D. Priyakumar, "Deep reinforcement learning for molecular inverse problem of nuclear magnetic resonance spectra to molecular structure," *The Journal of Physical Chemistry Letters*, vol. 13, no. 22, pp. 4924–4933, 2022.
- [24] N. Mazyavkina, S. Sviridov, S. Ivanov, and E. Burnaev, "Reinforcement learning for combinatorial optimization: A survey," *Computers & Operations Research*, vol. 134, p. 105400, 2021.
- [25] D. J. Mankowitz, A. Michi, A. Zhernov, M. Gelmi, M. Selvi, C. Paduraru, E. Leurent, S. Iqbal, J.-B. Lespiau, A. Ahern *et al.*, "Faster sorting algorithms discovered using deep reinforcement learning," *Nature*, vol. 618, no. 7964, pp. 257–263, 2023.
- [26] V. Mnih, K. Kavukcuoglu, D. Silver, A. A. Rusu, J. Veness, M. G. Bellemare, A. Graves, M. Riedmiller, A. K. Fidjeland, G. Ostrovski *et al.*, "Human-level control through deep reinforcement learning," *nature*, vol. 518, no. 7540, pp. 529–533, 2015.
- [27] R. S. Sutton and A. G. Barto, *Reinforcement learning: An introduction*. MIT press, 2018.
- [28] V. Mnih, K. Kavukcuoglu, D. Silver, A. Graves, I. Antonoglou, D. Wierstra, and M. Riedmiller, "Playing atari with deep reinforcement learning," *arXiv preprint arXiv:1312.5602*, 2013.
- [29] T.-Y. Kim, K. Kim, and J.-H. Kim, "Deep reinforcement learning based sar image pre-processing algorithm with finite buffer leo satellite networks," in *2022 13th International Conference on Information and Communication Technology Convergence (ICTC)*, 2022, pp. 2207–2209.
- [30] N. Xu, C. Huo, X. Zhang, Y. Cao, and C. Pan, "Hyperparameter configuration learning for ship detection from synthetic aperture radar images," *IEEE Geoscience and Remote Sensing Letters*, vol. 19, pp. 1–5, 2021.
- [31] A. Viros-i Martin, D. Selva, and R. Alimo, "Scheduling mission reconfiguration for an interferometry synthetic aperture radar using deep reinforcement learning," in *IGARSS 2020-2020 IEEE International Geoscience and Remote Sensing Symposium*. IEEE, 2020, pp. 6941–6944.
- [32] F. Xu and Y.-Q. Jin, "Bidirectional analytic ray tracing for fast computation of composite scattering from electric-large target over a randomly rough surface," *IEEE Transactions on Antennas and Propagation*, vol. 57, no. 5, pp. 1495–1505, 2009.
- [33] D.-X. Yue and F. Xu, "A coherent generative scheme for sar image representation," in *2021 IEEE International Geoscience and Remote Sensing Symposium IGARSS*. IEEE, 2021, pp. 427–430.
- [34] M. Zhang, Y. Zhao, J.-X. Li, and P.-B. Wei, "Reliable approach for composite scattering calculation from ship over a sea surface based on fbam and go-po models," *IEEE Transactions on Antennas and Propagation*, vol. 65, no. 2, pp. 775–784, 2016.
- [35] S. Fu and F. Xu, "Differentiable sar renderer and image-based target reconstruction," *IEEE Transactions on Image Processing*, vol. 31, pp. 6679–6693, 2022.
- [36] M. Hessel, J. Modayil, H. Van Hasselt, T. Schaul, G. Ostrovski, W. Dabney, D. Horgan, B. Piot, M. Azar, and D. Silver, "Rainbow: Combining improvements in deep reinforcement learning," in *Proceedings of the AAAI conference on artificial intelligence*, vol. 32, no. 1, 2018.
- [37] AFRL, "The air force moving and stationary target recognition database," pp. <https://www.sdms.afrl.af.mil/-datasets/mstar/>, 2016.
- [38] A. Kirillov, E. Mintun, N. Ravi, H. Mao, C. Rolland, L. Gustafson, T. Xiao, S. Whitehead, A. C. Berg, W.-Y. Lo *et al.*, "Segment anything," *arXiv preprint arXiv:2304.02643*, 2023.
- [39] K. He, X. Zhang, S. Ren, and J. Sun, "Deep residual learning for image recognition," in *Proceedings of the IEEE conference on computer vision and pattern recognition*, 2016, pp. 770–778.